

We are IntechOpen, the world's leading publisher of Open Access books Built by scientists, for scientists

4,800

Open access books available

122,000

International authors and editors

135M

Downloads

Our authors are among the

154

Countries delivered to

TOP 1%

most cited scientists

12.2%

Contributors from top 500 universities



WEB OF SCIENCE™

Selection of our books indexed in the Book Citation Index
in Web of Science™ Core Collection (BKCI)

Interested in publishing with us?
Contact book.department@intechopen.com

Numbers displayed above are based on latest data collected.
For more information visit www.intechopen.com



Nondestructive Evaluations by Using a Prototype of a Microwave Tomograph

R. Monleone, M. Pastorino, S. Poretti, A. Randazzo,
A. Massimini and A. Salvadè

Additional information is available at the end of the chapter

<http://dx.doi.org/10.5772/51488>

1. Introduction

In the field of nondestructive testing and evaluations (NDT&E), inspection systems working at microwave frequencies are now rather common (Zoughi, 2000; Franchois et al., 1998; Heinzelmann et al., 2004; Schilz & Schiek, 1981). They usually work by considering the electromagnetic waves reflected or transmitted by a body or a specimen. The percentage of reflection or the resulting attenuation of the waves can be correlated to the characteristic of the material or to possible defects inside the structure. Recently, tomographic approaches have been proposed, too. In this case, the imaging apparatus rotates around the target under test in order to collect multi-illumination multiview data. After a proper post-processing of the measured data, slides of the target cross section are obtained and visualized as rough images of the values of the retrieved dielectric parameters. The working modality is similar to the X-ray computerized tomography, but, at this lower frequency, the scattering phenomena is significant. Consequently, two approaches can be followed. The scattering contribution can be considered as an unwanted signal to be eliminated (see, for example, (Bertero et al., 2000)) or it can be included in the retrieving process (Colton & Kress, 1998). In the last case, which is considered in the present contribution, the field measured in a given position cannot be related to the transmitted field produced by a source located at an opposite position with respect to the unknown target. On the contrary, any measured value must be related to all the sources (if more than one illuminates the target contemporarily) and, mainly, to all the scattering points inside the target itself (i.e., the entire cross section).

In the last years there has been a growing interest in developing imaging systems working at microwave frequencies both for industrial applications (Kharkovsky & Zoughi, 2007; Giakos et al., 1999; Kraszewski, 1996) and medical diagnostics (Meaney et al., 2000; Jofre et al., 1990; Hagl et al., 2003; Henriksson et al., 2010).

In this Chapter, the development of a prototype of imaging tomograph working at microwave frequencies is discussed and reviewed (Salvadè et al., 2007, Pastorino et al., 2006). By using this prototype, dielectric targets can be inspected both for material characterization as well as for nondestructive analysis. The sample under test (SUT) is positioned on a rotating platform made by weakly scattering material, which represents the investigation area. Foam microwave absorbers surround the investigation area in order to minimize reflections due to the platform itself and to the motorized antenna actuators. A transmitting antenna is used for illuminating the SUT with a known incident electric field. The scattered electric field is collected by a receiving antenna, which can rotate around the table. Both antennas can be moved vertically and are mounted on fiberglass supports. The system can collect multi-illumination multiview data at different heights by means of log periodic transmitting and receiving antennas (8.5 dBi gain). Moreover, a multi-frequency acquisition is also performed by sweeping the operating band of 1-6 GHz with steps of 166 MHz at a sweep time of 96.348 msec. The transmitted wave and the samples of the scattered electric field are obtained by using a vector network analyzer (VNA) including a digital IF input filter configured at 300 Hz. The acquisition module is controlled by a custom software, while a standard LAN connection is used to interface the VNA to the management PC. Such PC also controls and synchronizes the movements of the antennas and the platform by means of three motorized actuators, whose drivers are connected through a CAN bus.

The Chapter is organized as follows. Basic concepts about the microwave measurement methods are briefly recalled in Section 2, whereas the design and the construction of the microwave tomograph prototype are discussed in Section 3. Section 4 provides some results obtained by inverting the measured data. Finally, some conclusions are drawn in Section 5.

2. Microwave measurement methods

Microwave imaging and inspection techniques are based on the interaction between electromagnetic fields and materials as defined by Maxwell's laws (Boughriet et al.; 1997; Fratticioli, 2001; Pozar, 2005; Vincent et al. 2004; Jeffrey et al., 1996). In particular, the propagation of microwaves is influenced by material properties such as the dielectric permittivity ϵ , the electric conductivity σ , and the magnetic permeability μ . Images obtained with microwave techniques are typically maps of the distribution of these parameters within an object or a material sample. In microwave sensing applications, it is usually assumed that $\mu = \mu_0$, being μ_0 the magnetic permeability of the vacuum (nonmagnetic materials), since inspection inside metals is very difficult to achieve due to their high conductivity (thus leading to very little penetration of microwaves). In general, for lossy materials, the propagation constant is expressed as (Balanis, 1989)

$$k = \alpha + j\beta = \sqrt{j\omega\mu(\sigma + j\omega\epsilon)} \quad (1)$$

where α and β are the attenuation and phase constants, respectively. It can be also introduced a complex permittivity, such that:

$$j\omega\epsilon_c = j\omega(\epsilon' - j\epsilon'') = \sigma + j\omega\epsilon = j\omega\epsilon \left(1 - j\frac{\sigma}{\omega\epsilon}\right) \quad (2)$$

where the imaginary part ϵ'' accounts for the material losses. For a homogeneous material, the complex permittivity can be easily determined by measuring the electromagnetic field (amplitude and phase) at two different positions (before and after crossing the material). More in general, when the material sample is not homogeneous and contains many zones with different properties, each change of property represents a discontinuity of ϵ_r and σ , giving rise to diffractions and reflections of the electromagnetic waves.

Various measurement techniques are known and well documented in the literature (Kraszewsky, 1996; Nyfors and Vainikainen, 1989; Clarke et al., 2003) for the characterization of dielectric properties of materials. Among these, the most popular are based on transmission, reflection, and resonant sensors. Systems working with transmission methods basically consist of a transmitting and one or more receiving antennas (Fig. 1). The material sample under test is placed between the antennas and interacts with the microwave propagation by modifying its amplitude and phase. The physical parameter that describes this variation is the propagation constant k which can be obtained by measuring the changes in attenuation and phase of the microwave signal when it passes through the material.

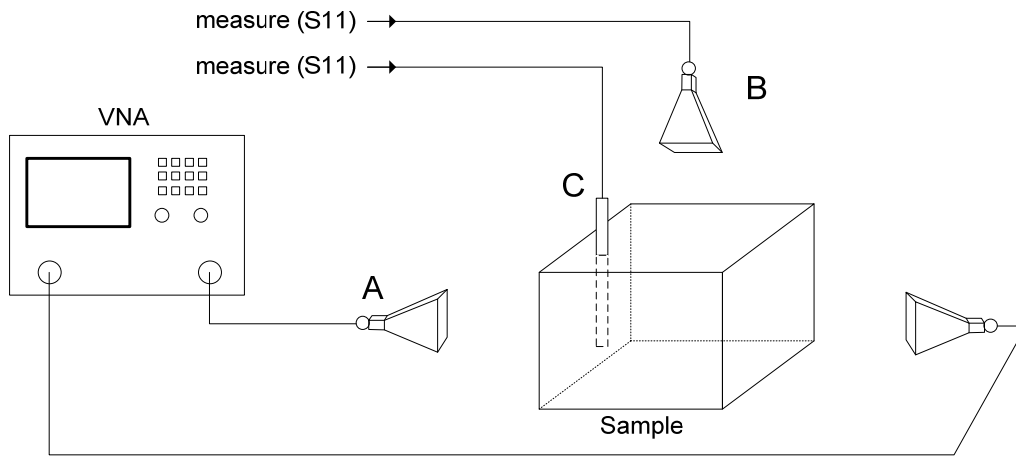


Figure 1. Microwave measurement configurations.

The measuring methods based on reflection concepts use one or more sensors that send a signal to a sample material probe and consequently analyze the amplitude and phase of the signal that is reflected back (or scattered). What is determined is the (complex) reflection coefficient Γ , which, for a normally incident plane wave impinging on an interface between two materials (e.g., the air and the unknown material) is given by (Jordan and Balmain, 1990; Balanis, 1989)

$$\Gamma = \frac{\eta_2 - \eta_1}{\eta_2 + \eta_1} = \frac{\sqrt{\epsilon_1} - \sqrt{\epsilon_2}}{\sqrt{\epsilon_1} + \sqrt{\epsilon_2}} \quad (3)$$

where η_2 and η_1 denote the intrinsic impedances of the two media (usually, medium 1 is air). When applying the reflection method, it is often useful to share the same antenna for both the transmitter and the receiver, therefore simplifying the mechanical complexity of the system. Examples of sensors based on this methodology are open-ended coaxial reflection sensors, monopole probe/antennas, open-ended waveguide sensors.

While microwave systems based on transmission and reflection concepts are now very common, systems based on microwave tomography are still rather infrequent. In a typical microwave tomograph setup, a material sample under test (SUT) is illuminated by a microwave source and the scattered field is collected by one or more receiving antennas placed at different positions around the SUT. The information of the scattered electric field is then used to obtain the dielectric properties inside the sample.

What is actually measured is the sum of the incident and the scattered fields. Since the incident field is known, the scattered field can be deduced. In order to collect as much information as possible about the scattered field, it is necessary to measure the total field at different locations. Also, the reconstruction algorithm requires that this procedure is repeated by illuminating the SUT with incident fields that arrive from different angles and directions.

The simplest configuration for a tomograph is therefore that with one moveable transmitting antenna and one moveable receiving antenna, similar to that of the transmission sensor previously described, but with the two antennas usually not facing each other. In order to reduce the amount of moving parts, an array of static antennas can also be used. The block diagram for the electronic hardware of a microwave tomograph with a single moveable antenna pair is shown in Fig. 2.

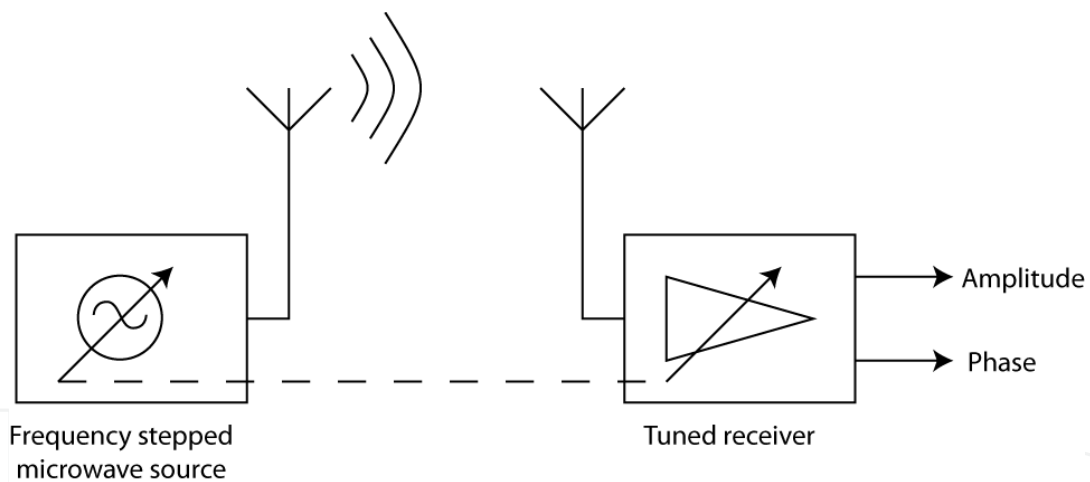


Figure 2. Simple block representation of a two-antenna tomographic set up.

The illuminating antenna is fed with a signal from a microwave generator working at one or more frequencies. The used wavelength should be chosen comparable to the electrical dimensions of the object to be analyzed. The receiver must satisfy the bandwidth requirements of the transmitter and must be able to tune to its instant frequency. In order to capture also the weakest scattered signals, the receiver should have a good sensitivity, dynamic range and selectivity. It should be possibly immune to strong interferers that may be present on other frequencies. The information sought for is the amplitude and phase of the signal picked up by the receiver antenna, compared to those of the transmitted signal. This information is typically extracted from the baseband of the receiver in the form of a complex signal.

The transmitter signal is, in many cases, a CW carrier, so that the wanted signal will be found at frequency zero (DC) at the output of the baseband block of the receiver. The receiver's task is that of converting the RF signal centered at the transmitter's frequency to baseband, with the best accuracy, dynamic range and possibly lowest noise. This can be accomplished with various receiver architectures. In the case of the superheterodyne (or heterodyne), the received RF signal, after some filtering and amplification, is first converted to an intermediate frequency (IF) by mixing (heterodyning) it with a local oscillator signal. Band (or channel) filtering is performed by a band pass filter in the receiver's IF section. Successively, the IF signal is demodulated into a base band signal by a synchronous demodulator (a mixer) or other circuits, based on the modulation type of the signal (e.g. envelope detector for an AM signal with carrier). Adequate RF filtering is therefore mandatory to block image frequencies.

For imaging applications not only the amplitude of the received signal, but also its phase is relevant. The phase information must therefore be preserved during the whole signal processing chain throughout the base band. To this end, the IF signal is converted to the base band with a vector (or I/Q) mixer as shown in Fig. 3.

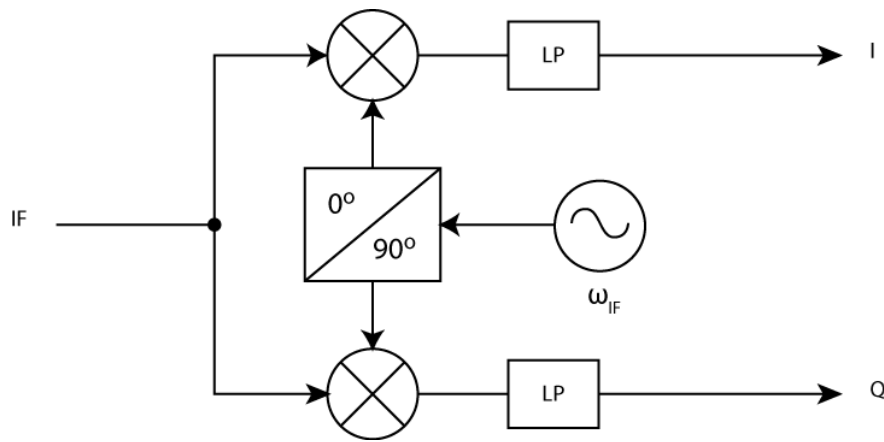


Figure 3. IF to baseband I/Q demodulator

A variant of the superheterodyne receiver aimed at mitigating the image frequency problem and used in multi-band receivers is an architecture with two consecutive IF frequency sections and mixers. The higher the chosen IF frequency, the larger the distance between the wanted RF and the unwanted RF image frequencies will be, therefore relaxing the constraint for the RF image blocking filter. On the other hand, in a multi-band receiver IF filtering is used to block adjacent channel signals. Such filtering becomes more difficult at higher IF frequencies, because the relative bandwidth of the IF filter will be smaller for a given channel width.

The double conversion receiver helps to avoid this compromise by first converting the RF signal to a higher IF (and therefore relaxing the front end filtering requirements), followed by a second converter and IF where the more demanding channel selection filtering is performed. Of the two local oscillators in a double conversion receiver, one is tunable and the other operates at a fixed frequency. A fixed frequency oscillator can be better optimized

for low phase noise and is also easier to implement. This makes it appealing as the first local oscillator in some single chip receivers. In this case, the absolute bandwidth of the first IF must cover that of all the RF channels, which for some applications (wide band receivers) might not be practical. Choosing the second IF at suitably low frequency enables the opportunity to demodulate the signal to baseband with a digital I/Q demodulator (see Low IF receiver).

An alternative to actively suppress the image frequency from the mixer output in a superheterodyne receiver is offered by an image reject or Hartley mixer, where RF image signals down converted by the two mixers forming this circuit arrive at the adder with opposite phase, therefore cancelling each other. On the other hand the wanted RF signals combine in phase. The effective image frequency rejection attainable by this circuit depends strongly on the accuracy of the 90° phase shifters and is therefore limited in practical situations, since it can be quite difficult to obtain sufficiently accurate 90° shifters at higher frequency.

The architecture using low IF receivers can be considered as a variant that is halfway between the superheterodyne receiver (of which it maintains the basic block diagram) and the homodyne receiver. It maintains the advantage of the superheterodyne over the homodyne consisting of the intrinsic absence of DC offsets in the demodulated signal but it also keeps the image frequency problem which must be addressed by some of the solutions discussed earlier. The low IF frequency makes it possible to digitize the signal at IF and perform the channel filtering and baseband conversion in the digital domain, which is an interesting feature from the system integration point of view. The better accuracy of the digital I/Q demodulator also increases the receiver's SNR in presence of complex signal modulation types.

However, the various receivers suffer in general from interfering signals, both in band and out of band but to a different extent. Self-generated interference due to LO or RF signal leakage from inside or nearby the receiver can be a source of concern with direct conversion receivers, whereas interference from RF signals at the image frequency are a known potential issue with superheterodyne receivers. Distortion due to nonlinear effects inside the receiver in presence of strong interfering signals is common to all practical receivers.

The distortion related to third order intermodulation products can be an issue in any type of receiver and can be generated by some nonlinearity at any stage, including the front end amplifier. In addition, second order intermodulation products generated inside the mixer of direct conversion receivers can directly translate to baseband also producing output distortions. It is therefore important that the receiver exhibits good performance concerning this point. The above mentioned effects result in practical limitations of real receivers in terms of dynamic range. Other issues derive from the unbalance in the analog quadrature networks found in many signal blocks discussed so far and can result in amplitude and phase errors of the baseband output signal. Finally noise from the local oscillators (phase noise), baseband noise and quantization noise occurring during the analog to digital conversion can reduce the signal to noise ratio of the output signal.

A laboratory prototype of a tomograph with good performance and flexibility can be built around a network analyzer. This type of instrument contains the necessary RF signal source, the RF receiver and baseband signal processing circuitry to obtain comparative amplitude and phase measurements between the source (illuminating) signal and the received (scattered) signal. As an example to show how different types of frequency conversion and receiver architectures discussed so far can be used and combined, the following Fig. 4 shows an example of a simplified network analyzer receiver's block diagram.

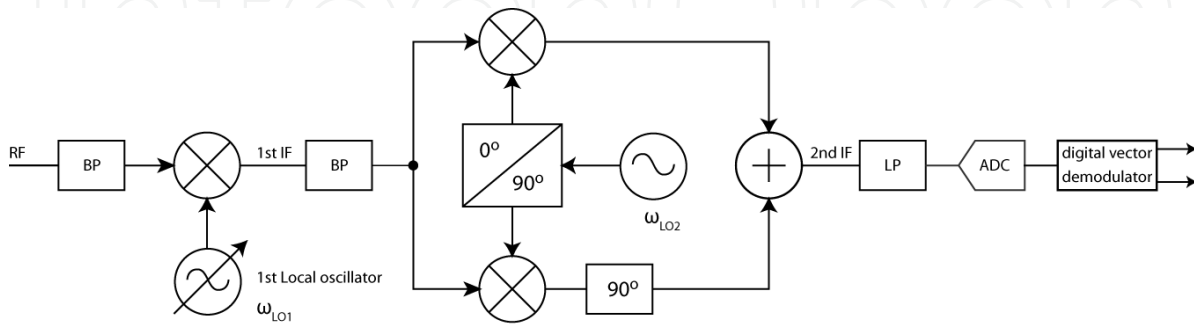


Figure 4. Simplified block diagram of the receiver section in a typical network analyzer

In this dual conversion receiver, the RF signal is downconverted to a first IF frequency by mixing it with a tunable local oscillator signal. Next, after some channel filtering, the signal is converted to a second low IF by means of an image reject mixer. At this point, the signal is digitized for further processing. The vector demodulation that will produce the amplitude and phase information is performed digitally. The source (transmitting) signal generation path is usually also made of one or more frequency translation (upconversion) steps in order to cover multiple frequency bands. Transmitter and receiver must be synchronized in phase and frequency.

From the previous discussion, it is evident that more than one receiver architecture is suitable for a microwave tomograph. The choice should then be made under consideration of the environment where the instrument is to be operated (interfering signals), complexity, cost and flexibility. Direct conversion receivers are probably the most flexible, since their frequency range is basically limited only by the local oscillator tuning range and because most of the signal processing can be done digitally. On the other hand, a laboratory prototype of a tomograph with optimal performance can be realized with the help of a commercial vector network analyzer (VNA), which is often based on a dual conversion superheterodyne receiver (Agilent, 2005). It is also very important, for a microwave tomograph, that extreme care is addressed against spurious emissions and parasitic couplings between antenna cables and circuit components (the latter are particularly critical in direct reception/homodyne receivers), as they could easily exceed the amplitude of weakly scattered signals coming from the SUT, thus severely reducing the SNR of the tomograph. To ensure low emissions or couplings from the antenna cables, these should be single or double shielded and the antennas should avoid signal injection on the cable shield.

Finally, the antenna is one of the most important component for microwave imaging systems. Theoretically, many kinds of antenna can fit in the tomography setup

specifications. In practical measurements, many things must be taken into account. According to the inversion algorithm needs, it is possible to select the optimal antenna characteristics that allow obtaining the best performance. In order to enhance the inversion accuracy many algorithms use multiple frequencies, some others use pulsed broadband signals. This requirement, for example, restricts the antenna choice to broadband types only. In the case of a two dimensional inversion algorithm, the SUT is assumed to be homogeneous and uniform along the z axis. In other words, the scatterer is divided into slices along this axis. Looking at the top view (Fig. 5(a)) the antenna radiation angle must be large enough to “illuminate” all the SUT surface. On the other hand, because of the properties of the inversion algorithm, the vertical radiation pattern (side view, Fig. 5(b)) must be taken as narrow as possible.

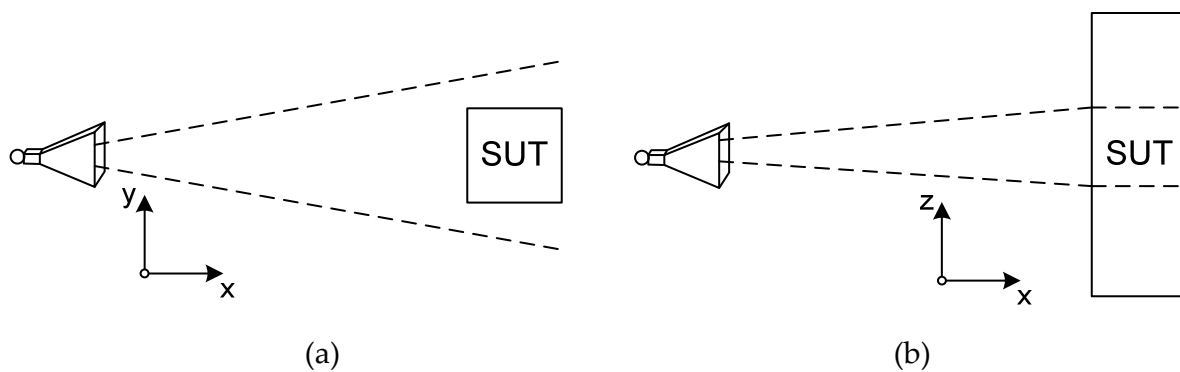


Figure 5. (a) Top and (b) side views of the SUT.

During the measurement setup design, it is also very important to consider the space surrounding the inspection area. The inversion algorithms usually assume this space to be perfectly homogeneous with known characteristics. In a real implementation this assumption is not valid. The measurement setup is composed by many mechanical components that could affect the measurements quality. A little variation of the surrounding volume can modify the measurements repeatability. The use of antennas with a limited back lobe can drastically decrease the influence of this problem. Another possibility to decrease the influence of the surrounding volume is the use of microwave absorbing materials surrounding the investigation area.

The choices of the number of antennas and their positions are extremely important. In this context there are many possible implementation options depending on the application needs and the inversion algorithm topology. One can distinguish mainly between two kinds of measurement setup: static or dynamic one. Each one brings advantages or disadvantages in relation to the specific application and the designer must therefore consider the properties of the object to be imaged. Depending on the SUT, it is generally possible to exclude right away some configurations. For example, in the case of a single piece that can fit entirely into the investigation domain, it is possible to perform a multiview inspection by rotating the SUT on its own axis instead of moving the illuminating antenna. On the other hand, if the goal is to measure only a part of a bigger object (e.g., parts of the human body, such as arms, legs or breast) the system has to perform a multiple view scanning without the SUT rotation.

3. Practical tomograph implementation example

This section describes the developed tomograph prototype (Fig. 6). In order to be as flexible as possible, a linearly polarized antenna with a large bandwidth has been chosen. Fig. 7 shows the considered antennas.

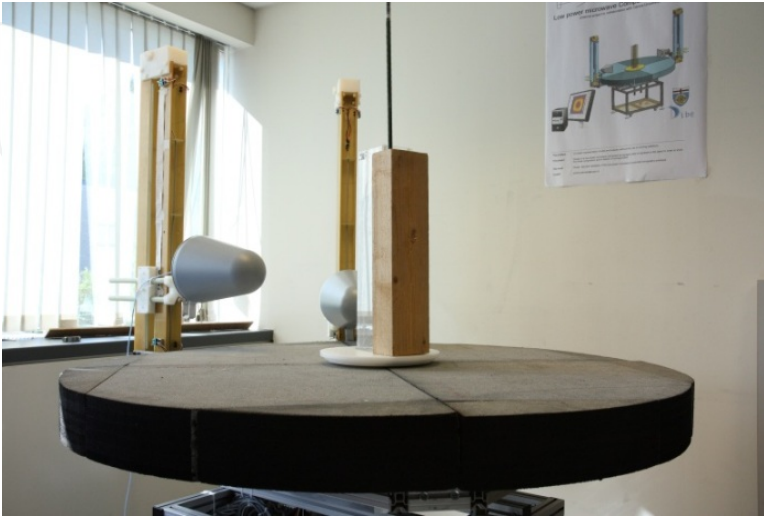
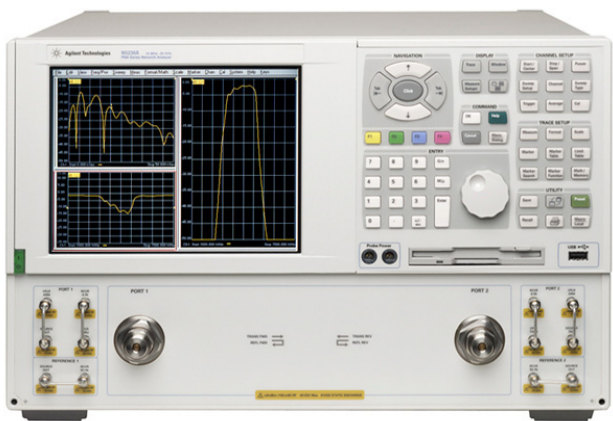


Figure 6. Prototype of the microwave tomograph (developed at SUPSI).

Antenna specifications	
Frequency range	850 MHz to 26.5 GHz
Polarization	Linear
Input impedance	50Ω
VSWR	≤ 2.5
Max. input power	10W to 2W
Gain	Typ. 8.5 dBi
Connector	PC 3.5 female

Figure 7. Rohde & Schwarz HL050 Antenna.

The generation, measurement and pre-processing of the microwave signal is carried out with a VNA, able to perform measurements from 10 MHz to 20 GHz. A managing software running on an external PC gathers all the measurement data through an Ethernet connection. The VNA generally requires a calibration. However, in a typical tomograph application, an empty (or void) reference measure is taken first and compared against subsequent measures with the SUT, therefore eliminating static errors due to reflections, phase adjustment errors, fixed interferers, and so on. Fig. 8 shows an example of the used VNA.



VNA Specifications	
Frequency range	10 MHz to 20 GHz
Max. output power	17dBm

Figure 8. Agilent VNA.

For mechanical reasons, some parts of the tomograph (in particular the basement) are composed by an aluminum structure. Therefore, microwave absorber material (Fig. 9 and Fig. 10) are used to prevent reflections.



Absorber specifications	
Frequency range	> 600 MHz
Reflectivity range	> -17dB
Thickness	11.4 cm

Figure 9. Eccosorb AN79

During the development of the measurement system, the planning of the illuminating signal power and receiver sensitivity play, as previously mentioned, an important role. A good dynamic range is the key for reliable and accurate measurements. The entire measurement chain can be represented with the block diagram reported in Fig. 11.

The main elements are:

- **VNA output power (typically -10 – 20 dBm):** usually the transmitted power level can be easily adjusted on the instrument. If needed, there is the possibility to add an external amplifier to increase the power level.
- **RF cable loss (typically 1 - 10 dB):** the signal amplitude loss due to the cable attenuation is variable in function of the investigation frequency band, of the cable quality and length.

- **Switching hardware loss (typically 1 - 5 dB):** the attenuation given by the switching hardware is variable and mainly depends on the board layout, the components used and the frequency band.
- **Tx/Rx antenna gain/loss (typically -2 – 10 dB of gain):** depending of the antenna type gain or loss are both possible.
- **VNA receiver sensitivity (typically -70/-100dBm):** the instrument's sensitivity level specifies the minimum possible signal amplitude required to obtain a reliable measurement. The environment noise level could also negatively affect this limit.
- **Investigation area:** the investigation area attenuation is the most critical section of the whole chain. In fact, while in every other block it is possible to correct the signal level by adding some amplification, this is not possible inside the investigation area. The inspection area is composed by the SUT and by its surrounding dielectric, which in most of the cases is air. Fig. 12 shows an example of a (rough) investigation area power budget including the antennas gain.

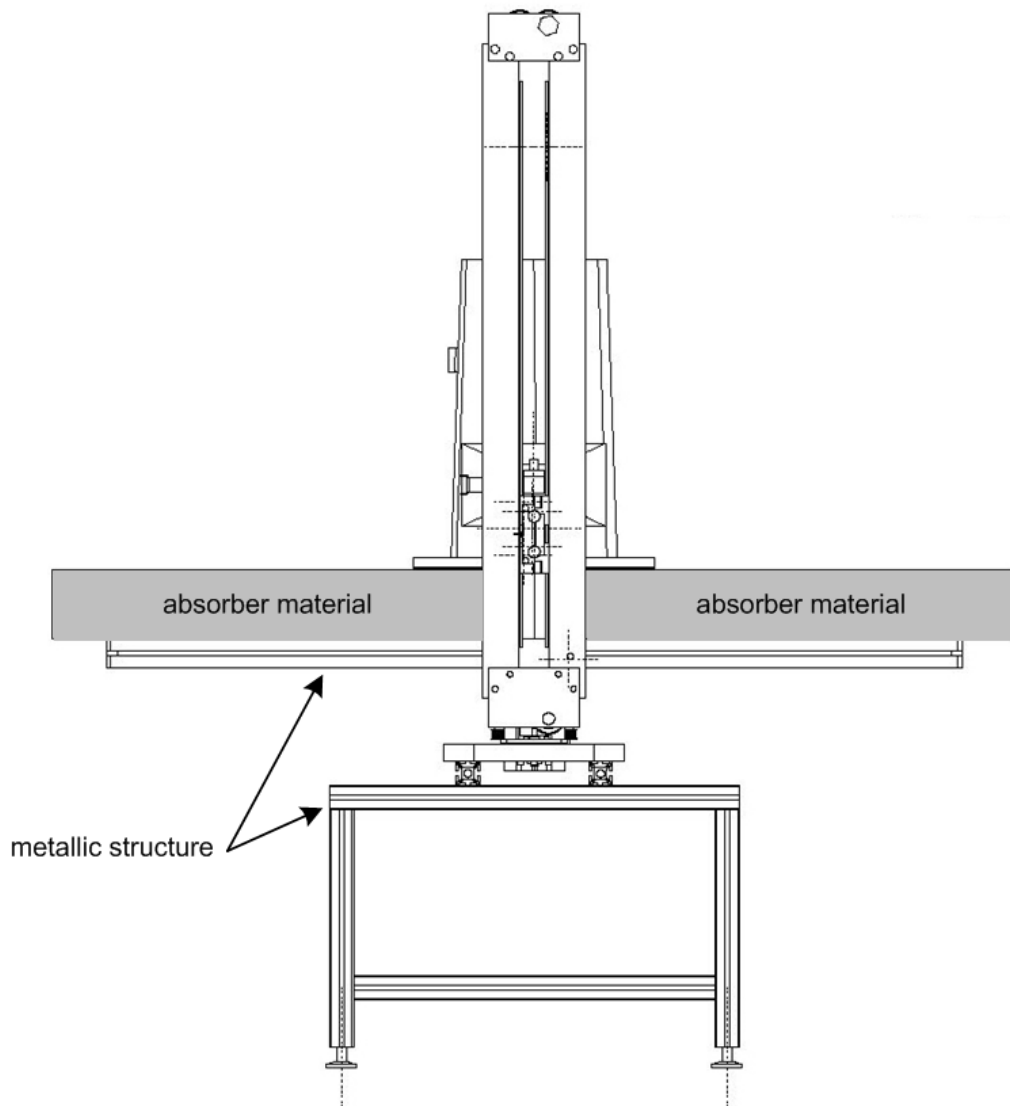


Figure 10. Absorber mounting.

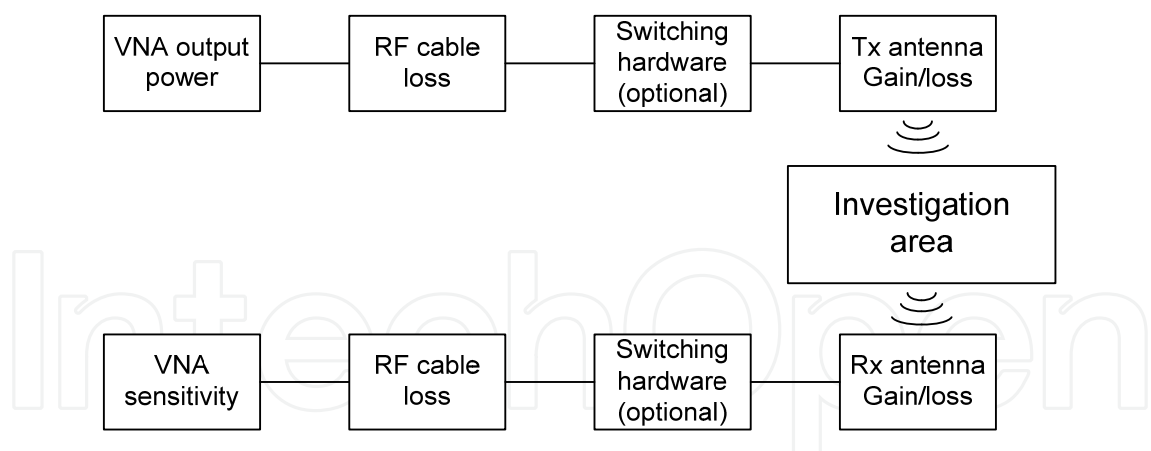


Figure 11. Measurement system block diagram

The most critical case is probably when the antennas are at a large distance and the SUT is relatively large. The specific example represents the attenuation of a SUT composed by wood ($\epsilon_r = 2.2$ and $\sigma = 0.045\text{ S/m}$).

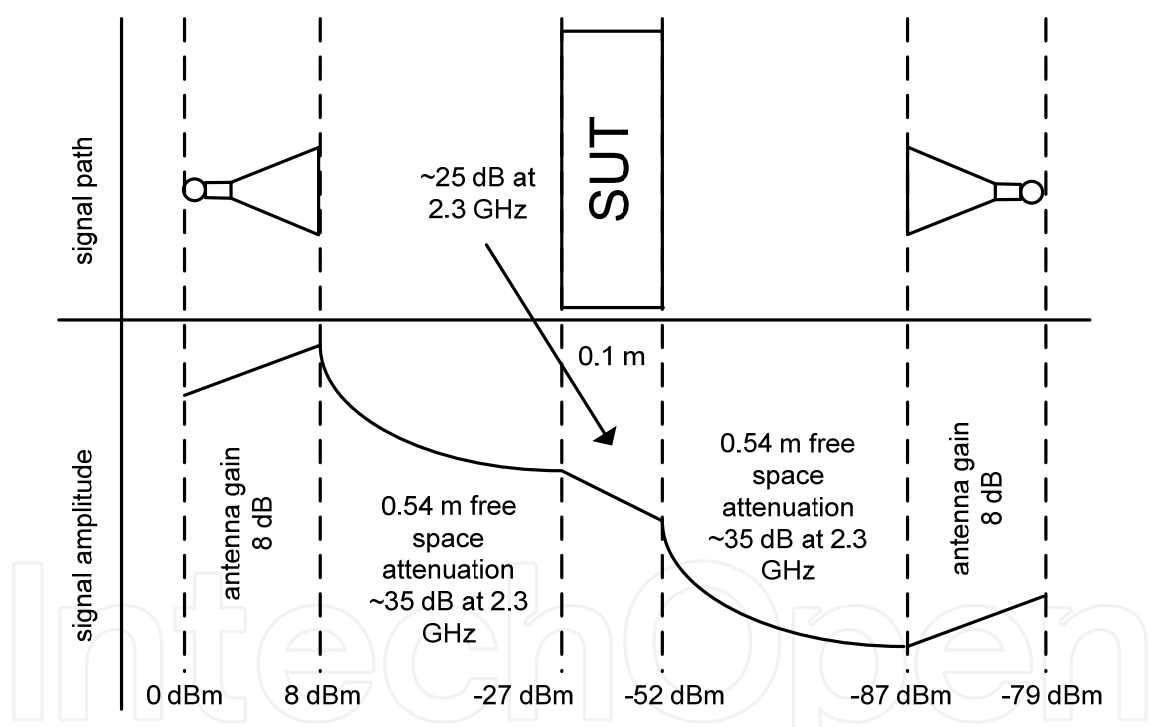
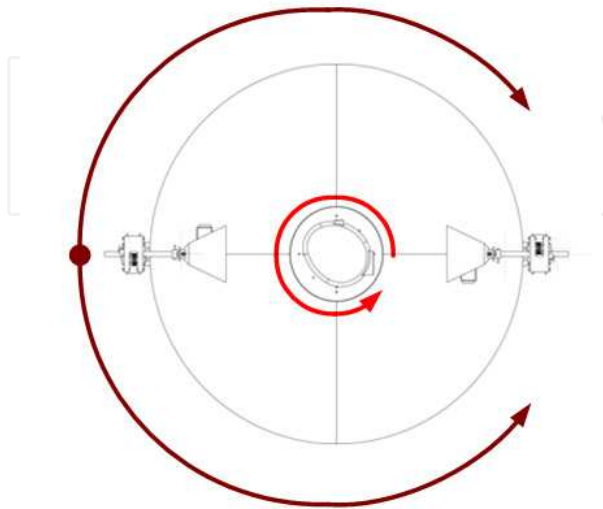


Figure 12. Simplified signal amplitude budget.

In order to acquire multiview data, in the developed tomograph prototype both the Rx antenna and the SUT are rotating and the Tx antenna is static (see the previous section). This choice leads to obtain data with the angular increments needed by the inversion algorithms. Future developments will be devoted to the implementation of a fully static design. The developed tomographic system (Fig. 6) is the result of various optimization steps. One of the major problems was the positioning accuracy of the servo motors in charge of moving the object and the Rx antenna. This accuracy should be an order of magnitude better than the required angular increments.



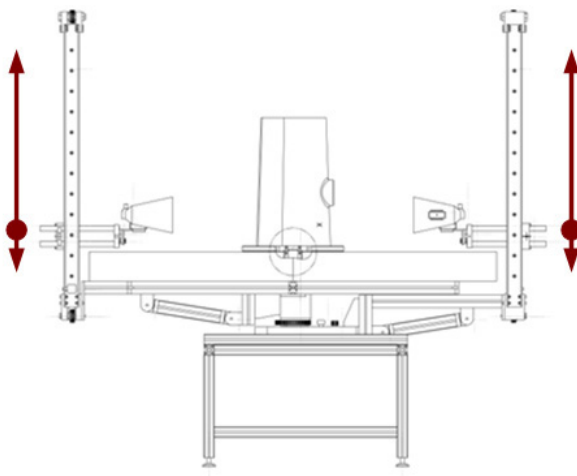
Parameters for the Rx antenna rotation:

- The Rx antenna can move from 45° to 315° with respect of the Tx antenna positioned at 0° .
- The minimum angular increment for the antenna rotation is 1° .

Parameters for the SUT rotation:

- The SUT can move 360° around its vertical axis.
- The minimum angular increment for the SUT rotation is 1° .

(a)



Parameters for the Rx and Tx antenna movements:

- Both antennas can move independently from 0mm to 750mm vertically.
- The minimum vertical displacement for the antennas is 1mm.

The horizontal distance of the antennas from the SUT is not under servo control but can be adjusted manually. This reduces the mechanical complexity and warrants a better stability of the entire tomograph.

(b)

Figure 13. (a) Horizontal circular movement (b) and horizontal and vertical linear movement of the developed prototype.

As mentioned, in order to keep the potential reflections as low as possible, the body of the tomograph was developed in such way that all the metallic parts can easily be hidden from the inspection area using absorbers (Fig. 10). Moreover, since covering the vertical arms with absorber was unpractical, these parts have been manufactured in glass resin. These precautions have made it possible to reduce the impact of the tomograph construction on the measured samples to a strict minimum at the benefit of better results.

A major drawback of this type of configuration is the time required to obtain a single image. First of all, each motor movement (summarized in Fig. 13) requires some travel and settling time. Consequently, as the measurement points increase, the number of time intervals needed for the motors to stabilize and for the network analyzer to acquire the signals and send the data to the computer increases, too. Table 1 shows the total time required for a full series of mechanical displacements of the Rx antenna corresponding to one view of the SUT. This time needs to be multiplied by the number of different views (angular positions) of the SUT.

Number of measurement points	Angular increment (in degrees)	Time (in minutes)
3	90	0.5
11	27	1.5
16	18	2
31	9	3.5
46	6	5
91	3	10

Table 1. Time consumption based on the mechanical positioning parameters.

The acquisition software developed for the management of the tomograph and running on a PC has to communicate with two different devices:

- the servo motor control units to provide position inputs and to read back status information;
- the VNA to input acquisition settings and to transfer the measures.

All steps involved in the acquisition procedure, i.e., a precise mechanical positioning, an accurate microwave measure, a lossless data transfer and storage need to be performed sequentially because an error free execution of each of them is necessary for a successful overall result. To address these requirements a simple but robust software has been developed (Fig. 14). It consists of a linear flowchart without parallelisms, which is flexible enough to allow adding checks after every step. The simplicity of the flowchart makes it possible to easily add processing blocks or functionalities in case of future needs. For a system prototype to be used during the design and validation of new imaging algorithms this was considered an important feature.

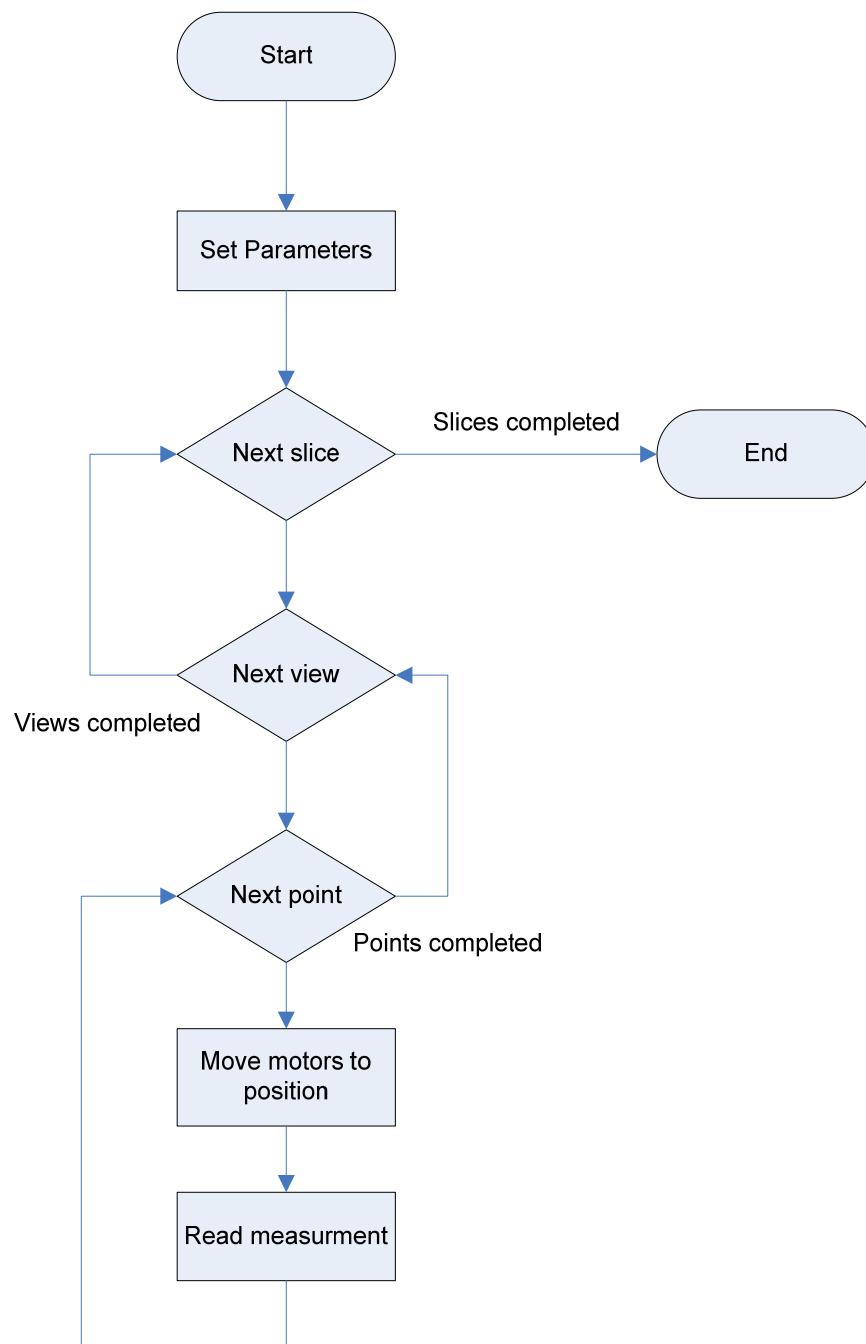


Figure 14. Acquisition software flowchart.

4. Measurement and simulation results

The measured data are stored and a processing method is applied in order to produce rough images of the reconstructed distributions of the dielectric parameters of the SUT cross section. The reconstruction procedure is based on the iterative application of the so-called distorted-Born approximation (Chew et al., 1994). Details concerning the implementation of the iterative procedures can be found in (Salvadè et al., 2010; Pastorino, 2010; Pastorino et al., 2006; Pastorino, 2004).

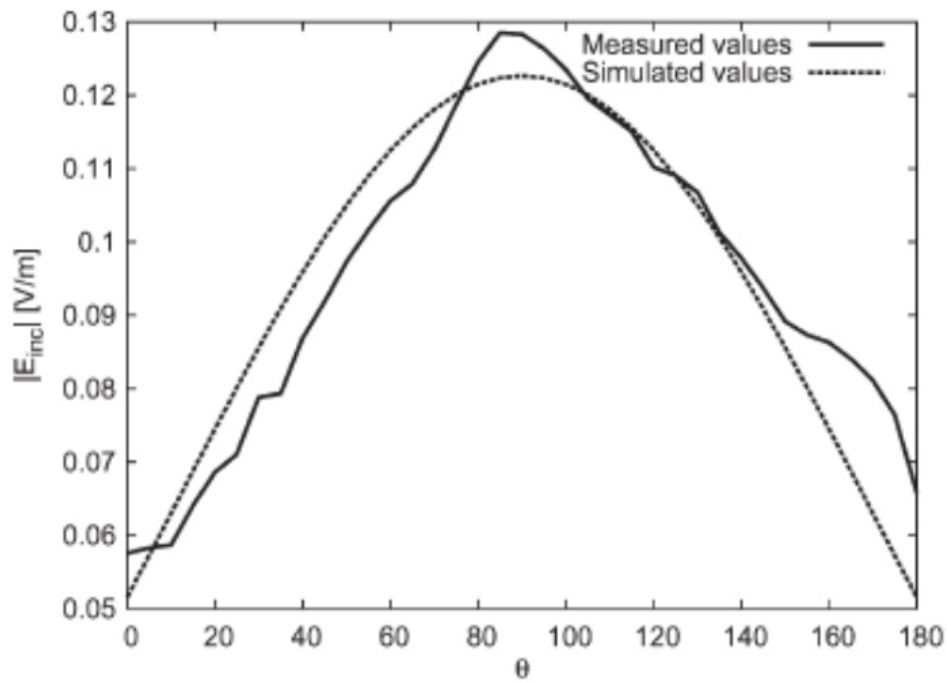
The capabilities of the proposed imaging systems have been preliminary assessed by means of comparisons with numerical results in terms of the measured electromagnetic field in the presence of scatters. The scatterer is a wood slab whose cross section has dimensions $11.7 \times 7.8 \text{ cm}$. A void circular hollow of radius of 2 cm has been drilled in the sample. The values of the dielectric parameters of the wood slab are about 2.2 (relative dielectric permittivity) and 0.04 S/m (electric conductivity). Fig. 15 and Fig. 16 provides the values of the measured and simulated samples. In particular, the figure plots refer to the amplitudes and phases of the incident (Fig. 15) and total (Fig. 16) electric fields, respectively. As can be seen, the measurements are in good agreement with the simulated values.

A lot of wood and plastic slabs have been reconstructed by using the proposed prototype. The capabilities of the approach in detecting voids and defects inside these structures have been also evaluated, even in the presence of noise and interfering signals. The reader can refer to papers (Salvadè et al., 2010; Monleone et al., 2012; Pastorino et al., 2009) and the reference therein. An example is reported in the following. The inspected target is composed by a hollow wood beam with rectangular cross section of $11.5 \text{ cm} \times 7.5 \text{ cm}$ and height of 50 cm (with a rectangular hole of size $5.5 \text{ cm} \times 3.5 \text{ cm}$) and a plastic object of $11 \text{ cm} \times 9 \text{ cm}$ and having the same height (with a rectangular hole of size $5.3 \text{ cm} \times 3.0 \text{ cm}$) containing sand. The nominal values of the relative dielectric permittivities of wood, plastic, and sand are 1.8, 2.7, and 3, respectively. An example of the reconstruction results obtained with a frequency of 4.5 GHz is reported in Fig. 17. As can be seen, the reconstruction is fairly good and both the hollow cylinders can be quite accurately located (inside the test area) and shaped. The values of the relative dielectric permittivity are also quite similar to the actual ones, confirming that the approach is able to provide a so-called “quantitative” imaging.

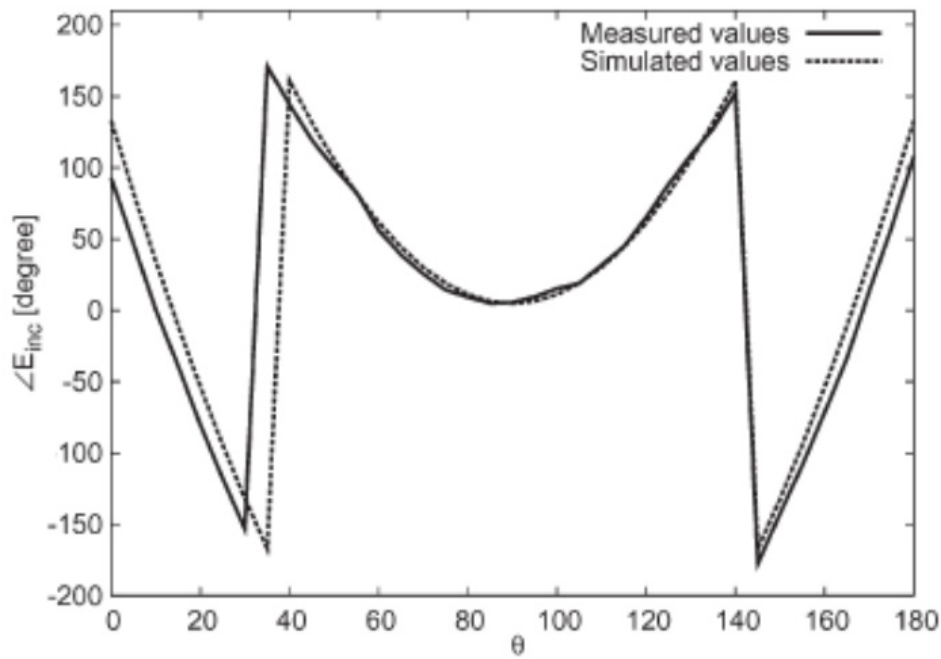
More recently, the presence of metallic inclusions inside a dielectric structure has been also considered (Salvadè et al., 2008; Maffongelli et al., 2012). In this case, the imaginary part of the contrast function is retrieved, since it is related to the electric conductivity distribution of the structure. The possibility of locating metallic inclusions inside dielectric objects is clearly very appealing in several industrial application, e.g., in the wood industry, where undesired metallic object can compromise the industrial process (the raw material can be not usable if foreign bodies are present). Moreover, these metallic inclusions may also damage the cutting machines used in that application.

Two examples are provided. In the first case, a wood slab of rectangular cross section of dimensions $11 \text{ cm} \times 9 \text{ cm}$ is assumed. Its relative dielectric permittivity is equal to $\epsilon = 2.2$ and its electric conductivity is equal to $\sigma = 0.045 \text{ S/m}$. For the considered scenario, 3 frequencies in the range $[3, 5] \text{ GHz}$ are assumed. Moreover, $V = 8$ sources, and $M = 51$ measurement points are considered. A single inclusion, modeled as a perfect electric conducting (PEC) metallic inclusion (i.e., $\sigma = \infty$) with circular cross section of radius $r = 1 \text{ cm}$ and located at $(2.0, 0.0) \text{ cm}$, has been considered.

The distribution of the electric conductivity $[\text{S/m}]$ provided by the inversion algorithm are shown in Fig. 18. Although, largely underestimated (no a priori information about the metallic nature of the scatterers have been included into the electromagnetic model), the distribution of the conductivity allows one to correctly identify the inclusion present in the wood slab.



(a)



(b)

Figure 15. Comparison between the measured and simulated incident electric fields at the measurement points. (a) Amplitude (in volts per meter). (b) Phase (in degrees). © [2009] IEEE. Reprinted, with permission, from M. Pastorino, A. Salvadè, R. Monleone, G. Bozza, and A. Randazzo, "A new microwave axial tomograph for the inspection of dielectric materials," *IEEE Trans. Instrum. Meas.*, vol. 58, no. 7, pp. 2072-2079, 2009.

In the second case, two buried objects, modeled as metallic inclusions with circular cross section of radius $r = 1 \text{ cm}$ and located at $(-2.0, 0.0) \text{ cm}$ and $(2.0, 0.0) \text{ cm}$, respectively, are

considered. In this case, too, the reconstructed distribution of the electric conductivity, shown in Fig. 19, allows a correct identification of the two inclusions.

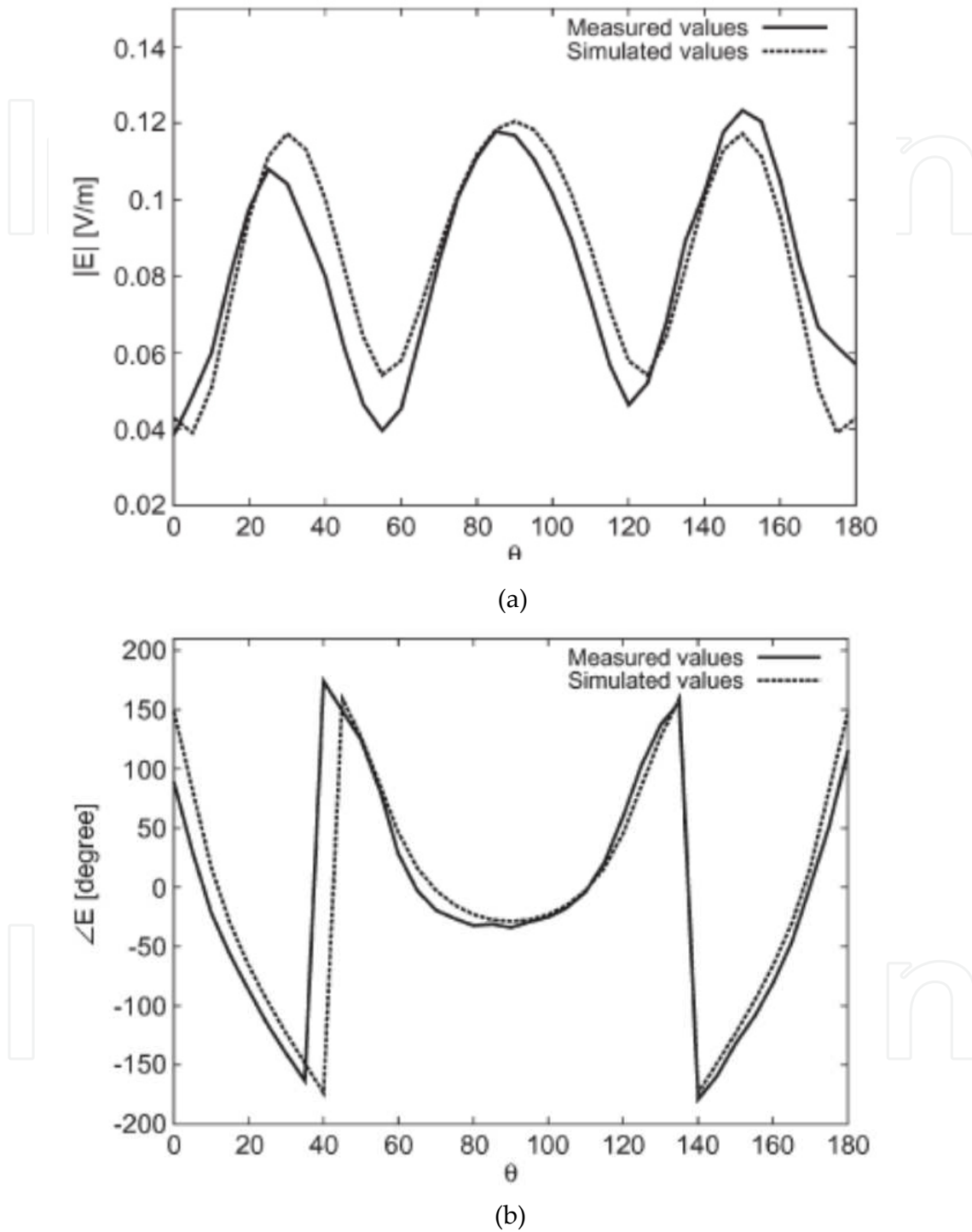


Figure 16. Comparison between the measured and simulated total electric fields at the measurement points. (a) Amplitude (in volts per meter). (b) Phase (in degrees). © [2009] IEEE. Reprinted, with permission, from M. Pastorino, A. Salvadè, R. Monleone, G. Bozza, and A. Randazzo, "A new microwave axial tomograph for the inspection of dielectric materials," *IEEE Trans. Instrum. Meas.*, vol. 58, no. 7, pp. 2072-2079, 2009.

5. Conclusions

In this paper, the development of a prototype of a tomographic imaging systems working at microwave frequencies has been reported. Starting with a brief review of microwave measurement concepts, the details of the designed system have been reported. Moreover, some measurements of the incident and total electric field have been provided, together with comparisons with simulated data. Finally, some reconstruction results concerning the

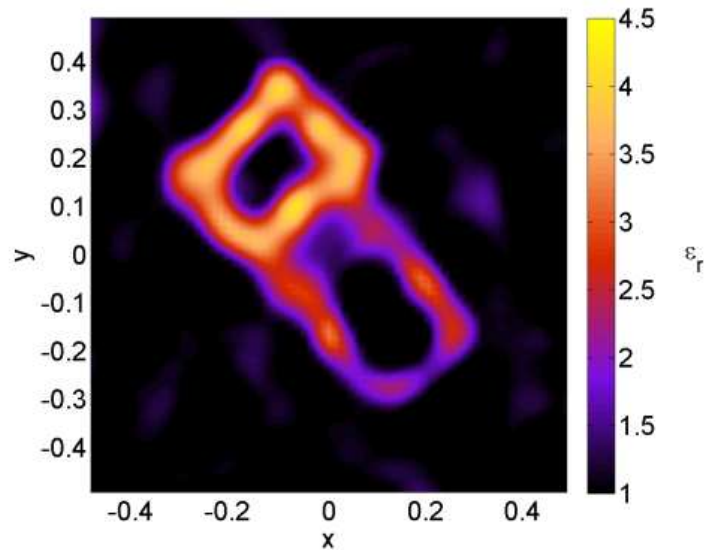


Figure 17. Reconstructed distribution of the dielectric permittivity of an inhomogeneous target (constituted by two hollow cylinders with rectangular cross sections, made of wood and plastic materials; one of them is filled by sand).

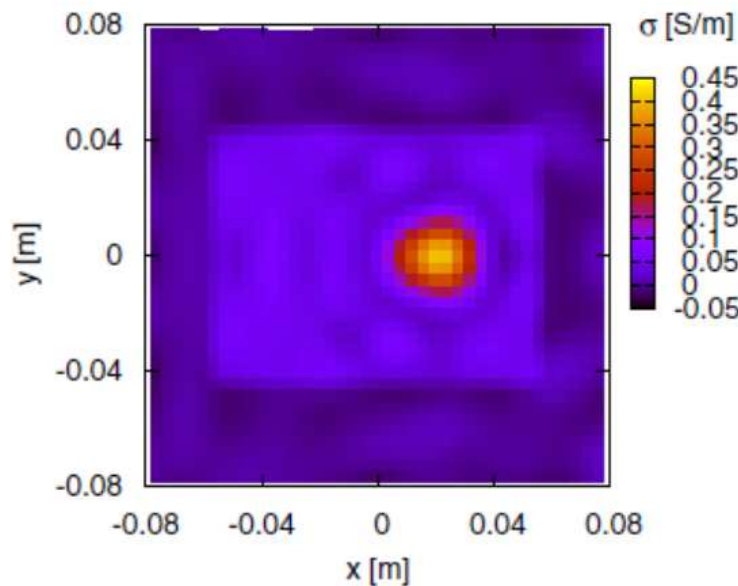


Figure 18. Reconstructed image of a wood slab with a metallic inclusion. © [2008] IEEE. Reprinted, with permission, from A. Salvadè, M. Pastorino, R. Monleone, A. Randazzo, T. Bartesaghi, G. Bozza, and S. Poretti, "Microwave imaging of foreign bodies inside wood trunks," *Proc. 2008 IEEE International Workshop on Imaging Systems and Techniques (IEEE IST08)*, Chania, Crete, Greece, Sept. 10-12, 2008.

inspection of dielectric material have been shown. The case of wood material with metallic inclusion has also been reported. Although quite preliminary, these results demonstrated that the inspection of these materials with microwave tomography is feasible. The developed system is quite simple and relatively inexpensive and can be further considered for application at several industrial levels, e.g., for nondestructive estimations in wood industry.

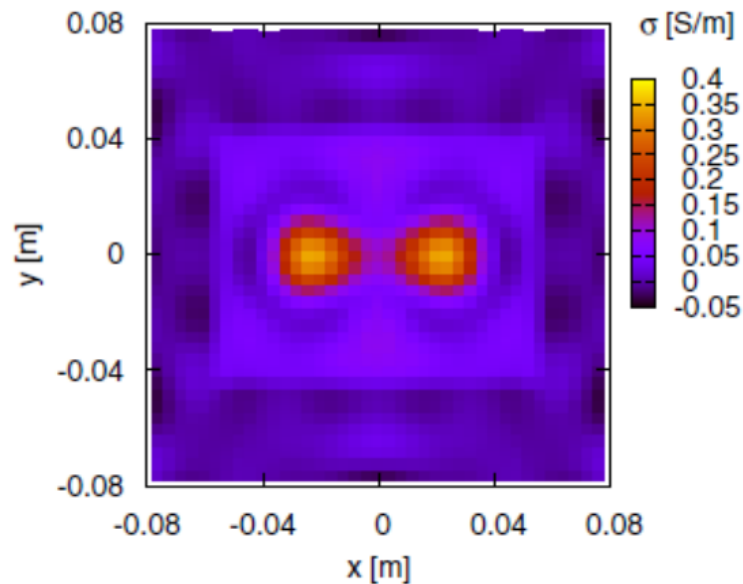


Figure 19. Reconstructed image of a wood slab with two metallic inclusions. © [2008] IEEE. Reprinted, with permission, from A. Salvadè, M. Pastorino, R. Monleone, A. Randazzo, T. Bartesaghi, G. Bozza, and S. Poretti, "Microwave imaging of foreign bodies inside wood trunks," *Proc. 2008 IEEE International Workshop on Imaging Systems and Techniques (IEEE IST08)*, Chania, Crete, Greece, Sept. 10-12, 2008.

Author details

R. Monleone, S. Poretti, A. Massimini and A. Salvadè

Department of Technology and Innovation, University of Applied Sciences of Southern Switzerland, Switzerland

M. Pastorino and A. Randazzo

Department of Naval, Electrical, Electronic and Telecommunication Engineering, University of Genoa, Italy

6. References

- Agilent (2005). Appl. Note 5989-2589EN: Basic of measuring the Dielectric properties of Materials.
- Boughriet, A. K.; Legrand, C. & Chapoton, A. (1997). Noniterative stable transmission/reflection method for low-loss material complex permittivity determination, *IEEE Trans. Microwave Theory Tech.*, vol. 45 (1997), pp. 52-57.
- Balanis, C. A. (1989). *Advanced Engineering Electromagnetics*, Wiley, NewYork, 1989.

- Bertero, M.; Miyakawa, M.; Boccacci, P.; Conte, F.; Orikasa, K. & Furutani, M. (2000). Image restoration in Chirp-Pulse Microwave CT (CP-MCT), *IEEE Trans. Biomed. Eng.*, vol. 47 (2000), pp. 690-699.
- Chew, W. C.; Wang, Y. M.; Otto, G.; Lesselier, D. & Bolomey, J.-C. (1994). On the inverse source method of solving inverse scattering problems, *Inv. Probl.*, vol. 10 (1994), 547-552.
- Clarke, R. N.; Gregory, A. P.; Cannell, D.; Patrick, M.; Wylie, S.; Youngs, I.; & Hill, G. (2003). A Guide to the characterization of dielectric materials at RF and microwave frequencies, The Institute of Measurement and Control, London, 2003
- Colton, D. & Kress, R. (1998). *Inverse Acoustic and Electromagnetic Scattering Theory*, Berlin, Springer-Verlag, 1998.
- Franchois, A.; Joisel, A.; Pichot, C. & Bolomey J.C. (1998). Quantitative Microwave Imaging with a 2.45Ghz Planar Microwave Camera, *IEEE Trans. Med. Imaging.* vol. 17 (1998), pp. 550-561.
- Fratticcioli, E. (2001). Characterization and development of a microwave industrial sensor for moisture measurements", Ph.D. Thesis, University of Perugia (Italy), 2001
- Giakos, G. C.; Pastorino, M.; Russo, F.; Chowdhury, S.; Shah, N. & Davros, W. (1999). Noninvasive imaging for the new century, *IEEE Instrum. Meas. Mag.*, vol. 2 (1999), pp. 32-35.
- Hagl, D. M.; Popovic, D.; Hagness, S. C., Booske, J. H. & Okoniewski, M. (2003). Sensing volume of open-ended coaxial probes for dielectric characterization of breast tissue at microwave frequencies, *IEEE Trans. Microwave Theory Tech.*, vol. 51 (2003), pp. 1194-1206.
- Heinzelmann, E.; Salvadè, A. & Monleone, R. (2004). Wavetester, die nicht invasive Schnüffelnase, *Tech. Rundsch.*, vol. 17 (2004), p. 50.
- Henriksson, T.; Joachimowicz, N.; Conessa, C. & Bolomey, J.-C. (2010). Quantitative microwave imaging for breast cancer detection using a planar 2.45 GHz system, *IEEE Trans. Instrum. Meas.*, vol. 59 (2010), pp. 2691-2699.
- Kharkovsky, S. & Zoughi, R. (2007). Microwave and millimeter wave nondestructive testing and evaluation—Overview and recent advances, *IEEE Instrum. Meas. Mag.*, vol. 10 (2007), pp. 26-38.
- Kraszewski (1996). *Microwave Aquametry*, IEEE press, 1996.
- Jeffrey, A.; Jargon & Janezic, M. D. (1996). Measuring complex permittivity and permeability using time domain network analysis, *Proc. IEEE Int. Microwave Symp.*, 17-21, June 1996, vol. 3, pp. 1407-1410.
- Jofre, L.; Hawley, M.; Broquetas, A.; de los Reyes, E.; Ferrando, M. & Elias-Fuste, A. (1990). Medical imaging with a microwave tomographic scanner, *IEEE Trans. Biomed. Eng.*, vol. 37 (1990), pp. 303-312.
- Jordan, E. C. & Balmain, K. G. (1990). *Electromagnetic waves and radiating systems*, PrenticeHall, Second Ed.
- Maffongelli, M.; Monleone, R.; Randazzo, A.; Pastorino, M.; Poretti, S. & Salvadè, A. (2012). Experimental reconstructions of dielectric targets with metallic inclusions by

- microwave imaging, Proc. Advanced Electromagnetics Symposium 2012 (AES'2012), Paris, France, April 16-19, 2012.
- Meaney, P. M.; Fanning, M. W.; Li, D.; Poplack, S. P. & Paulsen, K. D. (2000). A clinical prototype for active microwave imaging of the breast, *IEEE Trans. Microwave Theory Tech.*, vol. 48 (2000), pp. 1841–1853.
- Monleone, R.; Pastorino, M.; Fortuny-Guasch, J.; Salvadè, A.; Bartesaghi, T.; Bozza, G.; Maffongelli, M.; Massimini, A. & Randazzo, A. (2012). Impact of background noise on dielectric reconstructions obtained by a prototype of microwave axial tomograph, *IEEE Trans. Instrum. Meas.*, vol. 61, no. 1 (2012), pp. 140-148.
- Nyfors, E. & Vainikainen, P. (1989). *Industrial Microwave Sensors*, Artech House, 1989.
- Pastorino, M. (2004). Recent inversion procedures for microwave imaging in biomedical, subsurface detection and nondestructive evaluation, *Measurement*, vol. 36, no. 3/4 (Oct.–Dec. 2004.), pp. 257–269.
- Pastorino, M. (2010) *Microwave Imaging*, Wiley, Hoboken, 2010.
- Pastorino, M.; Salvadè, A.; Monleone, R.; Bozza, G. & Randazzo, A. (2009). A new microwave axial tomograph for the inspection of dielectric materials, *IEEE Trans. Instrum. Meas.*, vol. 58, no. 7 (2009), pp. 2072-2079.
- Pastorino, M.; Salvadè, A.; Monleone, R. & Randazzo, A. (2006). A Microwave Axial Tomograph: Experimental Set Up and Reconstruction Procedure, Proc. IEEE 2006 Instrum. Meas. Technol. Conf., Sorrento, Italy, Apr. 24–27, 2006, pp. 392–396.
- Pozar, D. (2005). *Microwave Engineering*, Third Ed., Wiley, 2005.
- Salvadè, A.; Pastorino, M.; Monleone, R.; Randazzo, A.; Bartesaghi, T. & Bozza, G. (2007). A Non-Invasive Microwave Method for the Inspection of Wood Beams, Proc. 3rd Int. Conf. Electromagn. Near-Field Characterization Imag. (ICONIC), St. Louis, MO, Jun. 27–29, 2007, pp. 395–400.
- Salvadè, A.; Pastorino, M.; Monleone, R.; Randazzo, A.; Bartesaghi, T.; Bozza, G. & Poretti, S. (2008). Microwave imaging of foreign bodies inside wood trunks, Proc. 2008 IEEE International Workshop on Imaging Systems and Techniques (IEEE IST08), Chania, Crete, Greece, Sept. 10-12, 2008.
- Salvadè, A.; Pastorino, M.; Monleone, R.; Bozza, G.; Bartesaghi, T.; Maffongelli, M. & Massimini, A. (2010). Experimental evaluation of a prototype of a microwave imaging system, Proc. 2010 URSI Commission B International Symposium on Electromagnetic Theory, Berlin, Germany, August 16-19, 2010, pp. 1108-1111.
- Schilz, W. & Schiek, B. (1981). Microwave Systems for Industrial Measurements, *Adv. Electron. Electron Phys.*, vol. 55 (1981), pp. 309–381.
- Vincent, D.; Jorat, L., & Noyel G. (2004). Improvement of the transmission/reflection method for dielectric and magnetic measurements on liquids between 0.1 and 20 GHz, *Meas. Sci. Technol.*, vol. 5 (2004), pp. 990-995.
- Zoughi, R. (2000). *Microwave Nondestructive Testing and Evaluation*, Kluwer, Dordrecht, The Netherlands, 2000.